

See discussions, stats, and author profiles for this publication at: <https://www.researchgate.net/publication/295394236>

Transient drag coefficients from a freely rising and falling solid sphere at moderate particle Reynolds numbers

Article in *The Canadian Journal of Chemical Engineering* · February 2016

DOI: 10.1002/cjce.22465

CITATIONS

0

3 authors, including:



Suresh Krishnan

SRM Institute of Science and Technology

8 PUBLICATIONS 45 CITATIONS

SEE PROFILE

READS

145



Balasubramanian Sivaswamy

SRM Institute of Science and Technology

2 PUBLICATIONS 0 CITATIONS

SEE PROFILE

TRANSIENT DRAG COEFFICIENTS FROM A FREELY RISING AND FALLING SOLID SPHERE AT MODERATE PARTICLE REYNOLDS NUMBERS

Suresh Krishnan,^{1*} Balasubramanian Sivasamy¹ and Karthikeyan Ramasamy²

1. Department of Chemical Engineering, SRM University, Kattankulathur, Tamil Nadu – 603203, India

2. Anjalai Ammal Mahalingam Engineering College, Kovil Venni, Thiruvavur District, Tamil Nadu – 614403, India

We performed numerical experiments on a freely rising and falling sphere in stagnant water for moderate particle Reynolds numbers ($130 \leq Re_p \leq 1091$) using spheres of various diameters and various sphere-water density ratios ($0.0016 \text{ m} \leq D_p \leq 0.004 \text{ m}$ and $0.08 \leq \rho_p/\rho_f \leq 1.92$). The methodology to carry out the arbitrary Lagrangian-Eulerian (ALE) moving mesh simulation technique was developed using ANSYS CFX[®] CFD software and the results obtained were validated with the experimental results published in the literature. The sphere trajectories, dynamics of sphere movement, and angular velocities play a significant role in transient drag coefficient. We observed that after maintaining a sphere diameter and dimensionless density difference ($\Delta\rho/\rho_f$) between water and a sphere at the same level as in the rising and falling sphere, the rising sphere attained terminal velocity faster than the falling sphere. The time required to keep the sphere inside the domain at a fixed distance from the rising and falling sphere decreased with increasing sphere diameter at a given $\Delta\rho/\rho_f$.

Keywords: CFD, fluid-particle dynamics, moving mesh simulation, sphere trajectory, angular velocity

INTRODUCTION

The hydrodynamics of a spherical particle moving relative to a stagnant fluid is important in many processes that involve two-phase (solid-liquid) systems. Understanding the particle motion during its transport through the fluid may enable us to estimate the particle residence time, the solid-fluid interphase momentum, and the heat and/or mass transfer rates. Practical applications involving two-phase interactions include fluidization, settling or rising particles in a fluid due to a density difference between fluid and particle, settling of particles in a gravity thickener, and bubbly flow reactors.^[1–4] The dynamics of particle movement is not the same in rising and falling spheres. The velocity of a rising or falling sphere in a stagnant fluid strongly depends on the drag force experienced by the sphere. The transient velocity and trajectory of a rising sphere were studied by Veldhuis et al.^[5] However, the rotation of the sphere was not measured due to experimental difficulties and it has been noted in few studies.^[5,6]

The present study addresses the behaviour of sphere motion and its effect on transient drag coefficient from a freely rising and falling sphere in stagnant water by using computational fluid dynamics (CFD) simulation. One of the major advantages of using numerical simulations compared to experiments is that we can study systems where controlled experiments are difficult to perform. Various authors have studied the behaviour of a sphere suspended in a fluid using advanced numerical simulation techniques.^[7,8,9] With such simulation techniques, the fluid flow is governed by the continuity and momentum equations coupled with an equation of motion of a rigid sphere. The arbitrary Lagrangian-Eulerian (ALE) simulation adopted in the present study is computationally expensive in order to capture the behaviour of the free motion of the spheres for a moderate particle Reynolds number (Re_p). When the Re_p increases, the quality of mesh around the sphere degrades within a shorter time. Frequent re-meshing of the fluid domain is essential to maintain an accurate flow field around the sphere.

Background and Scope

Considerable research has been invested in the past to understand the trajectories, time-averaged drag coefficient, and wake dynamics of a rising and falling sphere in a stagnant fluid. A brief review of recent literature on this phenomena is presented here.

The standard time-averaged drag coefficient correlations (fixed sphere in a fluid flow)^[10,11] that are used to determine the terminal velocity of a sphere are applicable only when the sphere moves in a vertical path at constant velocity without rotation through stagnant fluid.^[12] Rupesh et al.^[13] showed that the falling sphere in the stagnant fluid starts to rotate and triggers lateral migration when the sphere loses its axisymmetry at $Re_p = 210$. This results in a deviation of the drag coefficient from the standard drag curve.

Boillat and Graf^[14] observed that the drag coefficient for a smooth falling sphere in calm water is higher than the standard drag coefficient for fixed spheres tested in wind tunnels. They suggested doing further research to understand the discrepancy that exists between fixed sphere and falling sphere drag coefficients.

Mordant and Pinton^[15] experimentally estimated the velocity of a falling sphere in water at a temperature of 298 K using an acoustic method. At intermediate particle Reynolds numbers of a few hundred, the velocity of falling spheres with relatively lighter density showed oscillatory behaviour initially, which stabilized as time proceeded. This behaviour might be the reason behind the difference between a falling sphere and a sphere moving at a constant velocity (equivalently fixed sphere in a constant fluid

* Author to whom correspondence may be addressed.

E-mail address: suresh.k@ktr.srmuniv.ac.in

Can. J. Chem. Eng. 94:1003–1014, 2016

© 2016 Canadian Society for Chemical Engineering

DOI 10.1002/cjce.22465

Published online 31 March 2016 in Wiley Online Library

(wileyonlinelibrary.com).

flow). In this regime, the density of the sphere may be a control parameter. The reason behind the oscillatory behaviour of spheres has not been addressed by analytical or numerical techniques.

Jenny et al.^[16] numerically studied the instability (symmetry breaking bifurcation) on the velocity of a rising sphere and found trajectory deviation from vertical motion, which resulted in the effective increase of drag. This work was further extended to a wide range of Galileo numbers and density ratios of solid and fluid.^[17] They provided a chart of the different regimes (asymptotic state of trajectories) considering Galileo number and solid-fluid density ratio with a summary of numerical simulations.

Niazmand and Renksizbulut^[18] discussed the effect of rotation on drag coefficient by fixing a sphere under constant rotation in a fluid flow domain. The dynamic forces acting on the rotating sphere were studied numerically for Re_p up to 300 and dimensionless angular velocities up to $\Omega_z = 1$. They concluded that the variation in the time-averaged drag coefficient increases with increasing rotational speed at $Re_p > 50$.

Veldhuis et al.^[5] performed experiments on the behaviour of lighter rising and falling solid spheres in a stagnant fluid and determined the forces (drag and lift) experienced by the sphere using the Frenet reference frame. They observed the path of the rising sphere for a sufficiently long time because of chaotic trajectories, which resulted in a significant increase in the drag coefficient when compared to the standard drag. They concluded that the small difference between the measured drag and modelled drag may be due to rotation of the rising sphere, and it was due to limitations in the experimental method.

Horowitz and Williamson^[6] extensively studied the effect of particle Reynolds numbers ($Re_p = 100$ – $15\,000$) on the dynamics and wakes of freely rising and falling spheres for a wide range of mass ratios ($m^* = 0$ – 1.4). The mass ratio is defined as the relative density of spheres compared to the fluid. When $m^* < 1$, the sphere is rising in a stagnant fluid and when $m^* > 1$, the sphere is falling in a stagnant fluid. They observed rotation of the sphere at lower Re_p (450) for a rising sphere and no considerable angular velocity at higher Re_p (10 000). Above Re_p of 210, a constant time-averaged drag coefficient value close to 0.78 was reported, which is twice the value of the standard drag coefficient of a rising solid sphere in a fluid.^[5,6]

Based on the above studies, it is clear that the time-averaged drag coefficient significantly deviates from the standard drag coefficient due to the non-vertical trajectory and rotations of spheres in stagnant fluid, especially in a falling sphere with lesser density at intermediate particle Reynolds numbers (~ 210 – 1500). However, the reason behind the deviation in the time-averaged drag coefficient has not yet been studied. This paper begins with detailed comparisons of numerical simulation results with the experimental data available in the literature. Next, the simulation results are analyzed to examine the questions raised by Boillat and Graf^[14] and Mordant and Pinton.^[15] Finally, the effects of trajectory, rotation, and dynamics of sphere movement on the transient drag coefficient are reported by maintaining the sphere diameter and density difference between water and sphere at the same level for both falling and rising spheres.

PROBLEM FORMULATION FOR SPHERE MOTION IN STAGNANT WATER

Details of Domain and Mesh Adopted

A square-shaped duct with a height of 0.7 m was used to study sphere motion in stagnant water. A sphere was initially placed at a

distance of 0.1 m from the bottom of the duct for rising spheres and 0.1 m from the top of the duct for falling spheres. The sphere was considered to travel 0.45 m in the duct from its initial position for both falling and rising spheres. The blockage ratio, defined as the ratio between the sphere diameter and the breadth or width of the square domain, was maintained at ~ 0.01 to reduce the wall effect. Different sphere diameters (0.001 62 m, 0.0025 m, 0.003 m, 0.0035 m, and 0.004 m) were used in this study. A three-dimensional grid with non-uniform unstructured mesh was generated using the commercial ICEM CFX 13[®] CFD software. Around the sphere, finer mesh was generated to resolve rapid changes in velocities. The grid spacing went from smaller values near the sphere to larger values in the bulk. The prism layer was generated near the domain wall as shown in Figure 1.

Governing Equations

As the sphere moves in the stagnant water, the resulting deformation in the meshes surrounding the sphere was recorded while executing the simulations. The governing equations used are listed below.

i) Continuity equation:

$$\nabla \bullet V = 0 \quad (1)$$

ii) Momentum equation:

$$\rho_f \left(\frac{\partial V}{\partial t} + (V \bullet \nabla) V \right) = -\nabla P + \rho_f g + \mu \nabla^2 V \quad (2)$$

$$P = p + \rho_f g \bullet x \quad (3)$$

The governing equations on the fluid side Equations (1) and (2) were coupled with the equation of the motion of the particle to consider rotational and translational velocities for the particle. The equations describing the motion of the particle in a general three-dimensional case are as follows:

$$m \frac{dU_p}{dt} = m g + \int [-P1 + \tau] \bullet n \, ds \quad (4)$$

$$\frac{d(I \cdot \Omega_p)}{dt} = \int (x - X_p) \times ([-P1 + \tau] \bullet n) \, ds \quad (5)$$

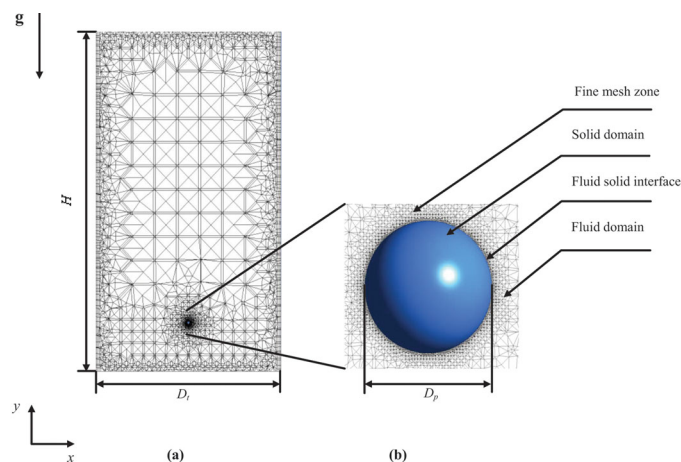


Figure 1. (a) Typical mesh generated for a rising sphere positioned at the centre of the fluid domain. (b) Magnified view of mesh around the spherical particle.

$$\mathbf{V} = \mathbf{U}_p + \boldsymbol{\Omega}_p \times (\mathbf{x} - \mathbf{X}_p) \quad (6)$$

where m is the mass of the sphere, \mathbf{U}_p is the translational velocity, $\boldsymbol{\Omega}_p$ is the angular velocity, $\mathbf{1}$ is the unit tensor, \mathbf{I} is the moment of inertia tensor, and \mathbf{X}_p is the coordinate of the centre of mass of the sphere. The mass of the sphere and moment of inertia were calculated using the following expressions: $m = \rho_p \pi D_p^3 / 6$ and $\mathbf{I} = \text{diag}(m D_p^2 / 10)$.^[8]

Initial and Boundary Conditions

Initially the water velocities inside the duct were set to zero. The sphere was then placed at the top (bottom) of the duct for falling (rising) simulations. Transient simulation was activated to track sphere motion inside the duct. Initially the sphere's linear and angular velocities were set to zero. The water and sphere velocities were updated in each time step by solving continuity and momentum equations along with the equation of motion. This updated information was used as a boundary condition for the next time step. The no-slip boundary condition was specified at the duct wall and sphere surfaces. The temperatures of water and sphere surfaces were set at 294 K. The properties of water at 294 K were incorporated in this simulation. The sphere density in each case of the simulations is presented in Table 1.

Mesh Motion Model

After integrating Equations (4) and (5) the sphere information was given to the mesh motion model^[19] as given in Equation (7) that determines the motion of nodes within the domain boundary. The displacement of nodes at the domain boundary was conveyed to other mesh points by solving the following equation:

$$\nabla \cdot (\Gamma_{diff} \nabla \alpha) = 0 \quad (7)$$

where α is the displacement relative to the previous mesh location and Γ_{diff} is the mesh stiffness, which determines the degree to which regions of nodes move together. Equation (7) was solved at the start of every coefficient loop of each time step in transient simulations. The displacement diffusion model for mesh motion retains the original relative mesh distribution around the sphere. For instance, if the initial mesh is relatively fine in certain regions of the domain (i.e. in the boundary layer), then it will remain relatively fine even after solving the displacement diffusion equation.

Arbitrary Lagrangian-Eulerian Moving Mesh Formulation

The motion of the sphere is based on translation and rotation along 3 dimensions. Hence, there are six degrees of freedom for movement of the sphere through the stagnant water. These simulations are computationally very expensive, especially when they are carried out in smaller time steps. During the simulation, the mesh quality can be determined by monitoring the orthogonality of the meshes. If the minimum orthogonality angle in the moving mesh domain is $< 35^\circ$ then re-meshing can be carried out.

The algorithm adopted for determining sphere translational and angular velocities in the water is presented below:

1. Provide fine, high-quality mesh around the stationary sphere inside the duct.
2. Solve the continuity and momentum equation to determine the hydrodynamic forces acting on the sphere from the established flow field.
3. Solve the equation of motion of the sphere that equates the rate of change of momentum of the sphere to the sum of the forces acting on it.
4. Determine the angular and linear velocities from the equation of motion.
5. Calculate the displacement of the sphere from the velocities obtained in step 4.
6. Solve the mesh motion model using the sphere displacement, and continue the simulations with previous flow field as an initial condition.
7. Check the mesh quality and redo the meshing when the minimum orthogonality angle in the domain is $< 35^\circ$, and repeat from step 2.
8. Terminate the loop once the sphere position reaches the specified point.

Solution Methodology

Fluid domain

The commercial CFD package ANSYS CFX V13[®], which is based on the finite volume method, was used to solve the governing Equations (1–3). The domain was defined in the global coordinate frame.

Discretization of the advection term

ANSYS CFX has optional schemes for selecting the discretization of the advection term. These schemes are upwind, high-resolution, and special blend factor. The high-resolution scheme was chosen for the discretization of the advection term of the momentum equations. It uses a non-linear recipe for blend factor at each node which maintains the blend factor as close as possible to unity without violating the boundedness principle (restricted to prevent nonphysical undershoots or overshoots in the solution).

Transient calculations

The transient calculations were carried out using the robust and bounded second-order backward-Euler scheme.

Pressure-velocity coupling

Rhie and Chow^[20] proposed a pressure correction scheme based on co-locating pressure and velocity at the same grid points. While interpolating velocities at the control volume face, an additional pressure correction term is added to the linear interpolation of velocities made between adjacent node velocities. This form of interpolation scheme is used to calculate the cell face velocity using local pressure gradients based on pressures at adjacent nodes rather than those at alternate nodes. The limitations imposed by checkerboard oscillations in pressure are overcome by this interpolation scheme. This in effect turns out to be a fourth-order pressure smoothing or dissipation that is added to the continuity equation.

Solution of the discretized equations

The momentum equations were first solved, using a guessed pressure field, and an equation for pressure correction was obtained. Due to the guess-and-correct nature of the linear system, a large number of iterations were necessary. Additionally, suitable

Table 1. Physical properties of fluid and solid spheres

Item no.	Parameters	Fluid	Solid
1	Density (kg/m ³)	998	79.8–1916.2
2	Viscosity (kg/m · s)	9.5808×10^{-4}	–

relaxation parameters had to be chosen to modify the correction to the previous iteration value of the variable. ANSYS CFX uses a coupled solver, which solves the hydrodynamics equations for velocities and pressure as a single system. To accelerate convergence when iteratively solving the linearized equations, a multigrid technique is adopted in ANSYS CFX. Detailed information is given in Neeharika et al.^[21] and the ANSYS CFX–Solver Theory Guide.^[19]

Solid sphere domain:

The equation of motion for a translating centre of mass of the sphere X , Equation (4), can be expressed as follows:

$$m \ddot{X} = F \quad (8)$$

where m is the mass, \ddot{X} is the rate of change of rigid body velocity, and F represents the sum of all forces which include mass of rigid body and explicit external force.

The rigid body solution algorithm uses a linear momentum solver for the translation of the rigid body and a separate angular momentum solver for the rotation of the rigid body. The linear momentum solver makes use of the Newmark integration scheme. The conventional Newmark integration scheme can be expanded as follows:

$$h_{n+1} = h_n + \Delta t \dot{h}_n + \Delta t^2 \left(\left(\frac{1}{2} - \beta \right) \ddot{h}_n + \beta \ddot{h}_{n+1} \right) \quad (9)$$

$$\dot{h}_{n+1} = \dot{h}_n + \Delta t \left((1 - \gamma) \ddot{h}_n + \gamma \ddot{h}_{n+1} \right) \quad (10)$$

where t is time, h is an entity such as spatial or angular position, and the subscripts n and $n + 1$ are the known solution at time t and unknown solution at time $t + \Delta t$ respectively.

Substituting Equation (8) for \ddot{X} into Equation (9) where h is replaced by translating centre of mass X and rearranging X_{n+1} is determined from the following:

$$X_{n+1} = X_n + \Delta t \dot{X}_n + \Delta t^2 \left(\left(\frac{1}{2} - \beta \right) \ddot{X}_n + \Delta t^2 \beta \left(g + \frac{F_{Ext}}{m} \right) \right) \quad (11)$$

From Equation (9), where h is replaced by X and rearranging \ddot{X}_{n+1} is determined from the following:

$$\ddot{X}_{n+1} = \frac{1}{\beta \Delta t^2} (X_{n+1} - X_n) - \frac{\dot{X}_n}{\beta \Delta t} - \left(\frac{1}{2\beta} - 1 \right) \ddot{X}_n \quad (12)$$

From Equation (10), where h is replaced by X and rearranging \dot{X}_{n+1} is determined from the following:

$$\dot{X}_{n+1} = \dot{X}_n + \Delta t \left((1 - \gamma) \ddot{X}_n + \gamma \ddot{X}_{n+1} \right) \quad (13)$$

The iteration of the above procedure is required to account for dependencies of the force on the position of the rigid body. The Newmark integration depends on two real parameters β and γ . These parameters are directly linked to the accuracy and stability of the Newmark time integration scheme. In this study, β and γ were chosen to be $1/4$ and $1/2$ respectively. This choice of parameters corresponds to a trapezoidal rule, which results in a second-order accurate scheme that is also unconditionally stable in linear analyses. Detailed information is given in the ANSYS CFX Solver Theory Guide.^[19]

The angular momentum solver makes use of the Simo Wong algorithm.^[22] This is a second-order time-stepping algorithm that exactly enforces conservation of total angular momentum. It uses a modified Newmark method given by $\beta = 1/2$ and $\gamma = 1$ to realize the second-order accurate integration.

The convergence criterion was fixed at a residual root mean square value of 10^{-4} . The time step value was < 0.001 s. It was chosen such that the root mean square (RMS) Courant number in the domain is sufficiently less than 0.5. The simulations were executed on an Intel[®] core (TM) i5-4570 CPU @ 3.20 GHz and 4 GB RAM running a Windows 7 platform. A significant amount of time was consumed for transient simulations, typically about 19 days for one case (falling or rising). Forty-eight cases with different sphere diameters and density ratios for rising and falling spheres in the stagnant water were investigated in this work.

Mesh Independence Test

A mesh independence test was carried out because of the tremendous computational resources required for domains with very small mesh sizes. In this work, the effect of different mesh sizes was studied in an extreme case, where the maximum possible particle Reynolds number was $Re_p = 1035$. The time-step value used in these simulations was 0.0006 s. The sphere velocities evaluated from the different mesh schemes are shown in Figure 2. The number of nodes used in the finer mesh scheme was almost twice that used in the coarse mesh scheme. The difference between the time-averaged y-directional sphere velocities in the two schemes was 2.79 % as shown in Figure 2. Further refinement in the mesh size could not be carried out due to limitations in computer resources. The typical mesh used in all the simulations consisted of 1.66×10^5 nodes. This is sufficient to capture the dynamics of sphere motion for a sphere < 0.004 m in diameter.

MATERIAL PROPERTIES AND DEFINITIONS

Material Properties

Physical properties of the water-solid sphere considered in this study are given in Table 1.

Dimensionless Density Difference ($\Delta\rho/\rho_f$)

The falling and rising nature of a sphere in stationary fluid is determined by the density ratio. The density ratio is defined as the ratio of the density of the sphere (ρ_p) to that of density of the fluid

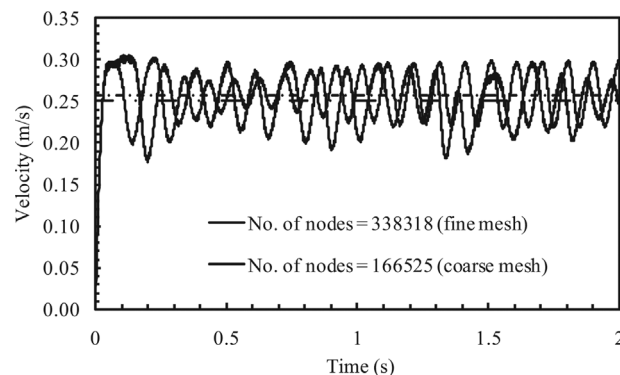


Figure 2. y -directional particle velocities with time for two different mesh sizes for the rising sphere case. Horizontal dotted lines are time-averaged values.

(ρ_f). When the density ratio is > 1 , the sphere moves downward from the top; if it is < 1 the sphere moves upward. In this study, the density difference between the water and sphere was kept the same for both rising and falling spheres and is defined in dimensionless form as given below:

$$\Delta\rho/\rho_f = \left| \frac{\rho_f - \rho_p}{\rho_f} \right| = \left| 1 - \frac{\rho_p}{\rho_f} \right| \quad (14)$$

Dimensionless Displacement of Sphere

The dimensionless displacement of a sphere is defined as the ratio of displacement of the sphere in X, Y, and Z directions (Dx , Dy , and Dz) to that of diameter of the sphere (D_p) as given below:

$$X = \frac{Dx}{D_p}, \quad Y = \frac{Dy}{D_p}, \quad \text{and} \quad Z = \frac{Dz}{D_p} \quad (15)$$

Time-Averaged Terminal Velocity ($\langle u_t \rangle$)

The velocity of the rising or falling sphere (u_t) through stagnant fluid was obtained from the simulation results by considering the sphere velocity against the direction of gravity or toward the direction of gravity. When the rising or falling sphere ceases to accelerate and continues to fall or rise at a constant velocity, the sphere has achieved terminal velocity, also called time-averaged terminal velocity. However, there were some instances in the present study during which the sphere's velocity changed with time due to dynamic wake structure interaction with the sphere after attaining a constant velocity. For these cases, the time-averaged terminal velocity was calculated once the sphere velocity reached a constant value (acceleration of sphere becomes zero) from the initial position as shown in Figure 3.

Particle Reynolds Number (Re_p)

The particle Reynolds number is defined as follows:

$$Re_p = \frac{D_p \langle u_t \rangle \rho_f}{\mu} \quad (16)$$

Local Drag Coefficient (C_d)

In the case of a rising or falling sphere, the drag coefficient was estimated by substituting the value of u_t at any given time in the following equation:

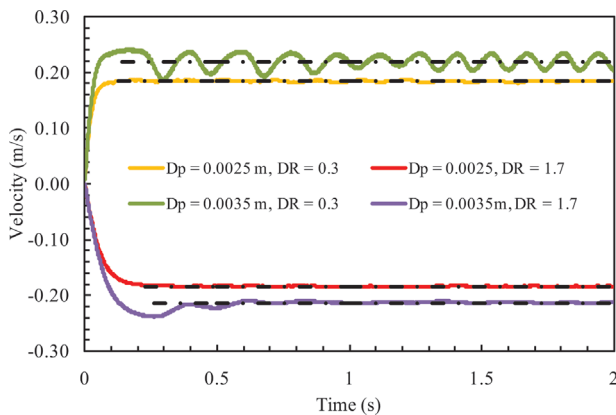


Figure 3. y-directional particle velocities with time at different particle diameters and density ratios (DR). Horizontal dotted lines are time-averaged values.

$$C_d = \frac{4gD_p\Delta\rho}{3\rho_f u_t^2} \quad (17)$$

Time-Averaged Drag Coefficient ($\langle C_d \rangle$)

The time-averaged drag coefficient was calculated using $\langle u_t \rangle$ of a sphere in the following equation:

$$\langle C_d \rangle = \frac{4gD_p\Delta\rho}{3\rho_f \langle u_t \rangle^2} \quad (18)$$

Dimensionless Sphere Surface Pressure (C_p)

C_p is defined as follows:

$$C_p = \frac{p_s - p_\infty}{\frac{1}{2}\rho_f V_s^2} \quad (19)$$

p_∞ is a reference pressure, which is chosen such that C_p at the front stagnation point is unity.^[23] V_s is the front stagnation velocity of rising and falling spheres in stagnant water. This method of scaling with respect to the stagnation point helped to compare pressure distribution around the rising and falling sphere.

Local Friction Factor (f)

The Darcy friction factor (f) is defined as follows:

$$f = \frac{4\tau_w}{\frac{1}{2}\rho_f V_s^2} \quad (20)$$

where τ_w is wall shear stress and can be obtained directly in the post-processing step of ANSYS CFX[®] used in the present work.

Terminal Velocity from Standard Drag Correlation

Cheng^[12] discussed the procedure to determine the terminal velocity of a sphere. The procedure was derived from a fixed sphere in a fluid flow approach. This procedure may be suitable for a sphere moving freely through stagnant fluid in a vertical path at constant velocity without rotation. The drag correlation proposed by Turton and Levenspiel^[10] given in Equation (21) was used in the procedure to estimate the terminal velocity and the residence time by specifying the distance travelled by the sphere in the fluid.

$$\langle C_d \rangle = \frac{24}{Re_p} \left(1 + 0.173 Re_p^{0.657} \right) + \frac{0.413}{1 + 16300 Re_p^{-1.09}} \quad \text{for } Re_p < 2 \times 10^5 \quad (21)$$

RESULTS AND DISCUSSION

Validation of CFD Simulation

The simulations were carried out for different diameters and density ratios with a blockage ratio of ~ 0.01 for both falling and rising spheres. The time-averaged drag coefficient ($\langle C_d \rangle$) results obtained through the simulation were plotted as a function of particle Reynolds number for both rising and falling spheres in the stagnant water, along with a previous control from experimental studies as shown in Figure 4.

We observed that the drag coefficients for a sphere moving freely agreed with the standard drag coefficient up to Re_p of 210 as reported by Jenny et al.^[16] and Rupesh et al.^[13] The density ratios varied from 0.7–0.3 for rising spheres and 1.3–1.7 for falling

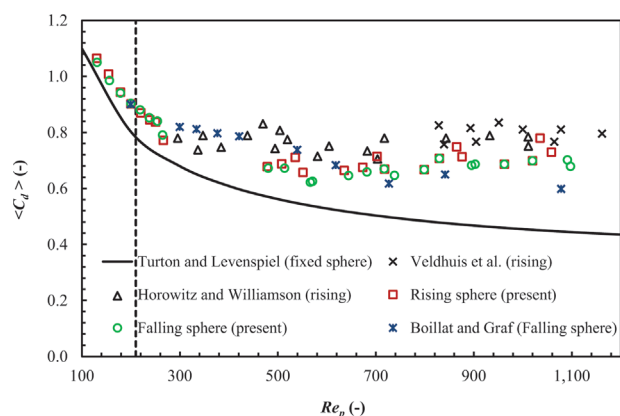


Figure 4. Comparison of time-averaged drag coefficients with literature values. Vertical dotted line is the breaking of axisymmetric wake in the fixed sphere case.

spheres at a diameter of 0.0016 m. The $\langle C_d \rangle$ for rising and falling spheres obtained under these conditions with particle Reynolds number < 210 are within 8 % of the values given by a standard drag coefficient curve for a sphere.^[10] We also observed that the percentage deviation of drag coefficient further rises with an increase in Re_p . This may be attributed to an increase in angular velocities and trajectory deviation from a vertical motion with increasing Re_p , as shown in Figures 5–9.

The $\langle C_d \rangle$ values started to deviate from the standard drag values when Re_p increased beyond 210 for smaller density ratios from 0.3–0.08 for rising spheres and larger density ratios from 1.7–1.92 for falling spheres at different sphere diameters. A sphere rising through stagnant water exhibits a non-vertical trajectory and rotates, and so takes a longer path inside the domain, as shown in Figures 6 and 8. Similar observations were reported by Veldhuis et al.^[5] and Horowitz and Williamson.^[6] At the lowest density ratio ($\rho_p/\rho_f = 0.08$), the $\langle C_d \rangle$ values were higher (0.74–0.77) compared to the other density ratios in rising spheres (0.3, 0.2, and 0.1) at a given sphere diameter.

The maximum discrepancies of the present simulation from the experimental values (Veldhuis et al.,^[5] Horowitz and Williamson,^[6] and Boillat and Graf^[14]) expressed in percentages are given in Table 2. For the rising sphere the present simulation and experimental value agree, as shown in Table 2. However, the simulation results of a falling sphere reveal higher drag coefficients than for Veldhuis et al.^[5] with the maximum difference being 20 %. The density ratios (1.4, 2.4, and 2.6) considered by Veldhuis et al.^[5] are not comparable with the present simulation results ($1.7 \leq \rho_p/\rho_f \leq 1.92$) even though the particle Reynolds numbers are almost the same. Similarly, the published experimental data concluded that the light density of the falling sphere at intermediate Re_p may be a controlled parameter (Mortan and Pinton^[15]). In contrast, the present drag coefficient of the falling sphere obtained under these conditions ($1.7 \leq \rho_p/\rho_f \leq 1.92$, $450 \leq Re_p \leq 1091$) exhibits a satisfactory match with the experimental data reported by Boillat and Graf.^[14]

For a falling sphere, the drag coefficient values occurred very close to and equal to those of the rising sphere, even though the trajectories of falling spheres in a stagnant fluid were shown to be oblique or intermediately oblique in nature (Figures 7 and 9). However, the x -directional rotation of the sphere was higher for a falling sphere compared to a rising sphere, as shown in Figure 5.

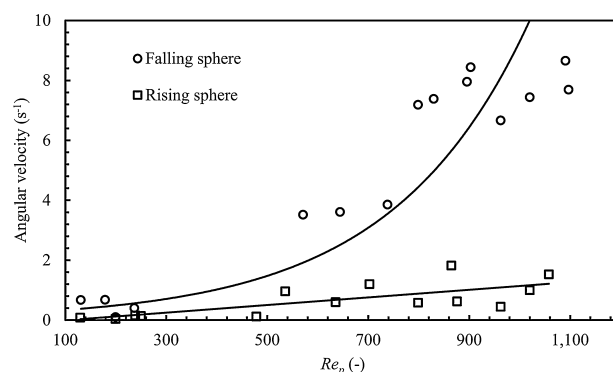


Figure 5. x -directional time-averaged angular velocity with particle Reynolds numbers for falling and rising cases.

Trajectories of the Rising and Falling Spheres

The instantaneous variation of y -directional sphere velocity is represented in a three-dimensional trajectory for three different diameters (0.0025 m, 0.003 m, and 0.0035 m) and two different dimensionless density differences between a sphere and water ($\Delta\rho/\rho_f = 0.7$ and 0.92) as shown in Figures 6–9. At $\Delta\rho/\rho_f$ of 0.92 in the rising sphere, most of the trajectories are found to be helical and the corresponding y -directional velocity varies significantly per cycle of a path when compared with $\Delta\rho/\rho_f$ of 0.7. However, the path is nearly a zigzag for $\Delta\rho/\rho_f$ of 0.7. In both cases, the velocities were maximum when the spheres turned from their path and the velocity was relatively lower in other regions as shown in Figures 6 and 8. The trends of velocity and trajectory from these numerical simulations agree closely with experimental results reported by Veldhuis et al.^[5]

In the falling sphere, the trajectories were oblique or intermediately oblique for $\Delta\rho/\rho_f$ of 0.92 and 0.7 at three different sphere diameters of 0.0025 m, 0.003 m, and 0.0035 m, as shown in Figures 7 and 9. The particle Reynolds numbers for these cases varied from 478–910. The trends of trajectories obtained under these conditions agree with experimental trends published by Horowitz and Williamson.^[6]

Angular Velocity of the Rising and Falling Spheres

The time-averaged x -directional angular velocity was relatively larger when compared with y - and z -directional angular velocity in both rising and falling spheres in stagnant water. At $Re_p \leq 260$, the time-averaged x -directional angular velocity was predicted to be lower and was comparable between rising and falling spheres, as shown in Figure 5. At this stage, the angular sphere velocity has not contributed much to the enhanced time-averaged drag coefficient compared with the standard drag coefficient (Figure 4). From the fixed sphere case, unsteady three-dimensional flow with vortex shedding starts at $Re_p > 270$.^[24] Once the wake behind the sphere lost its axisymmetry with vortex shedding around the sphere, the rising sphere ($\rho_p/\rho_f < 1$) triggered a helical or zigzag path (Figures 6 and 8) and exhibited lower time-averaged angular velocities (Figures 10a, 11a, 12a). In contrast, the falling sphere ($\rho_p/\rho_f > 1$) has a higher time-averaged angular velocity (Figures 10a, 11a, 12a) in an oblique or intermediate oblique path (Figures 7 and 9). The time-averaged x -directional angular velocity increased rapidly with Re_p for the falling sphere, whereas it varied linearly with Re_p for the rising sphere, as shown in Figure 5. Thus, for the falling sphere, the enhanced drag coefficient was mainly due to angular velocity. However, for the

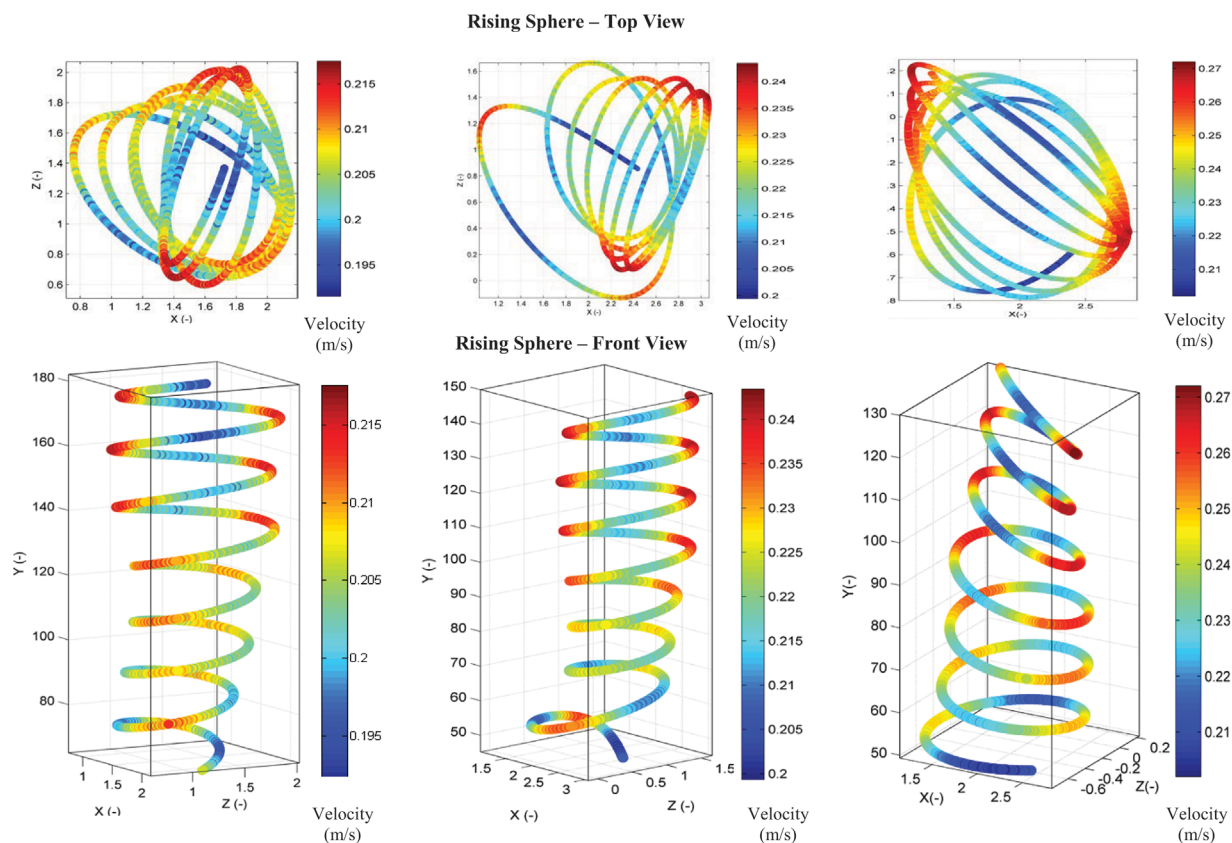


Figure 6. 3-D trajectories with y-directional velocity of a sphere rising in water at $\Delta\rho/\rho_f = 0.92$ for different sphere diameters of 0.0025 m, 0.003 m, and 0.0035 m.

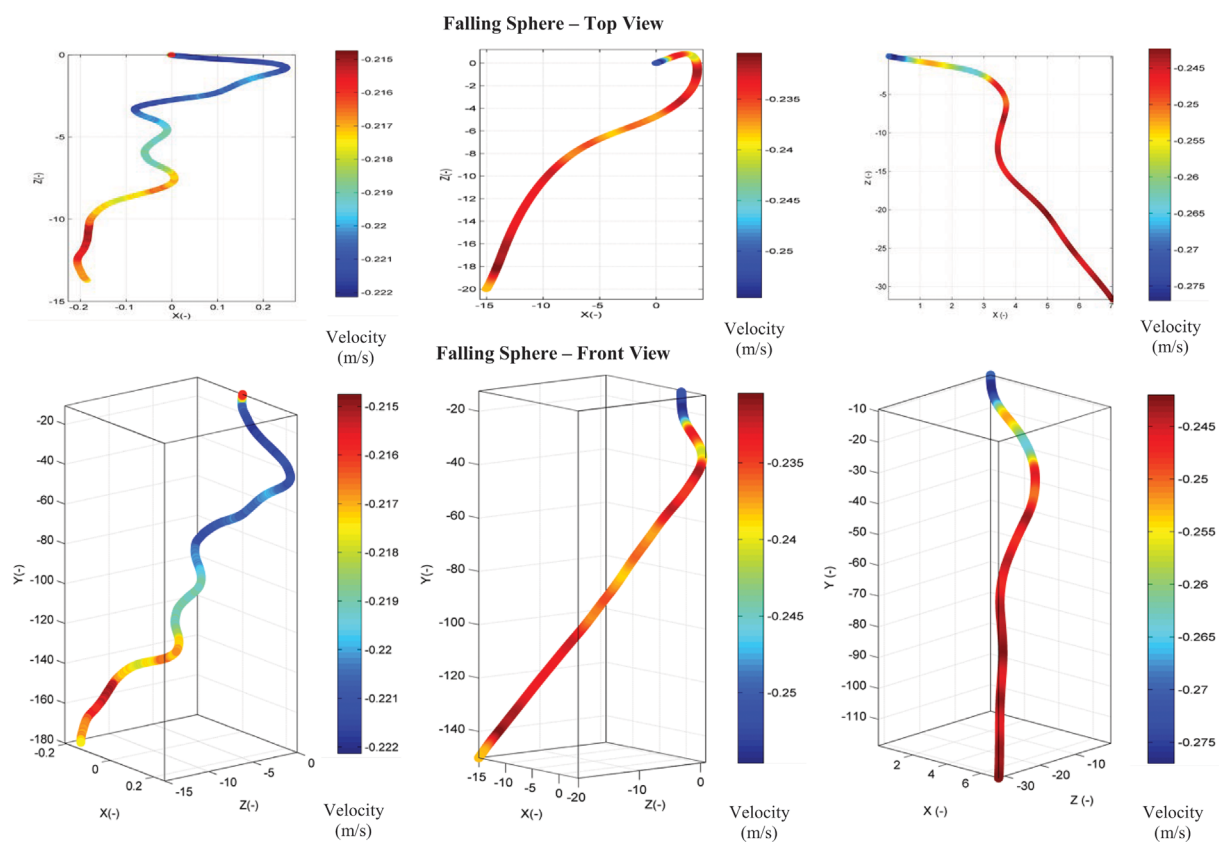


Figure 7. 3-D trajectories with y-directional velocity of a sphere falling in water at $\Delta\rho/\rho_f = 0.92$ for different sphere diameters of 0.0025 m, 0.003 m, and 0.0035 m.

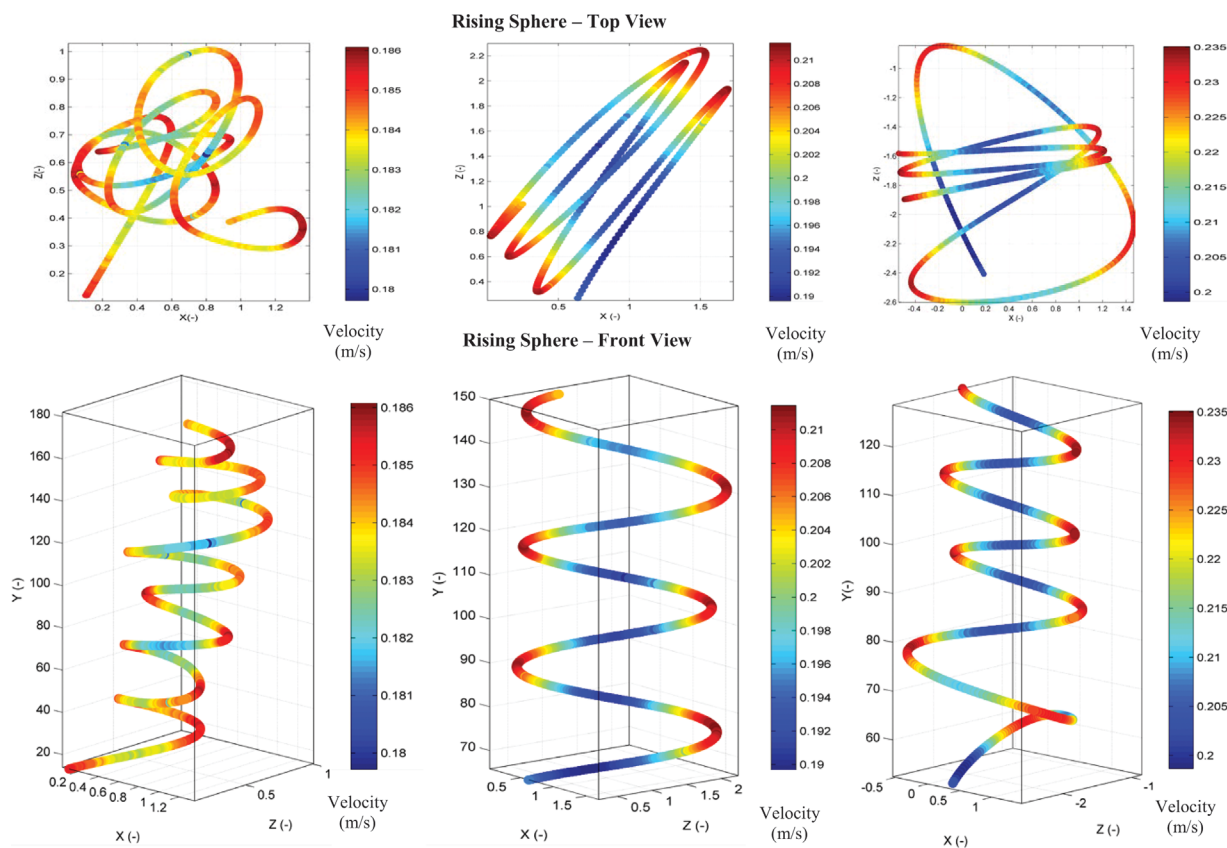


Figure 8. 3-D trajectories with y -directional velocity of a sphere rising in water at $\Delta\rho/\rho_f=0.7$ for different sphere diameters of 0.0025 m, 0.003 m, and 0.0035 m.

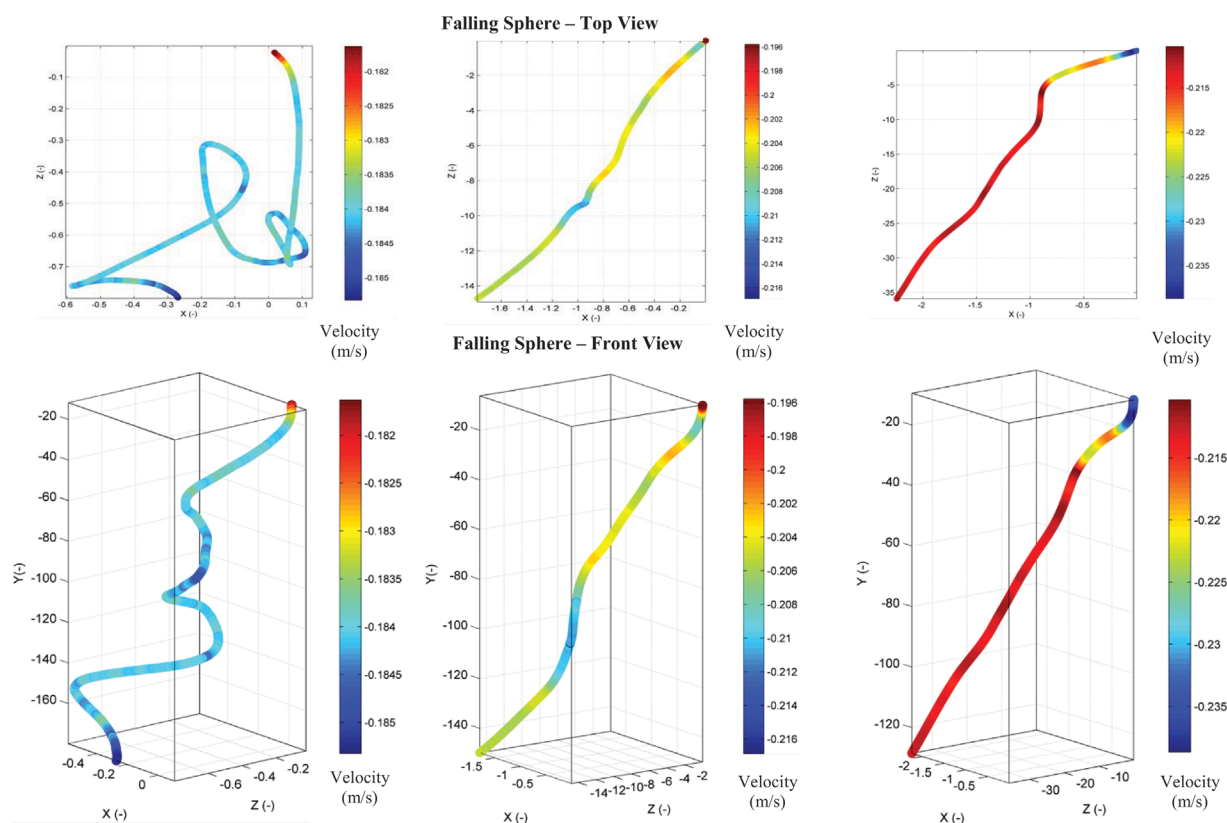
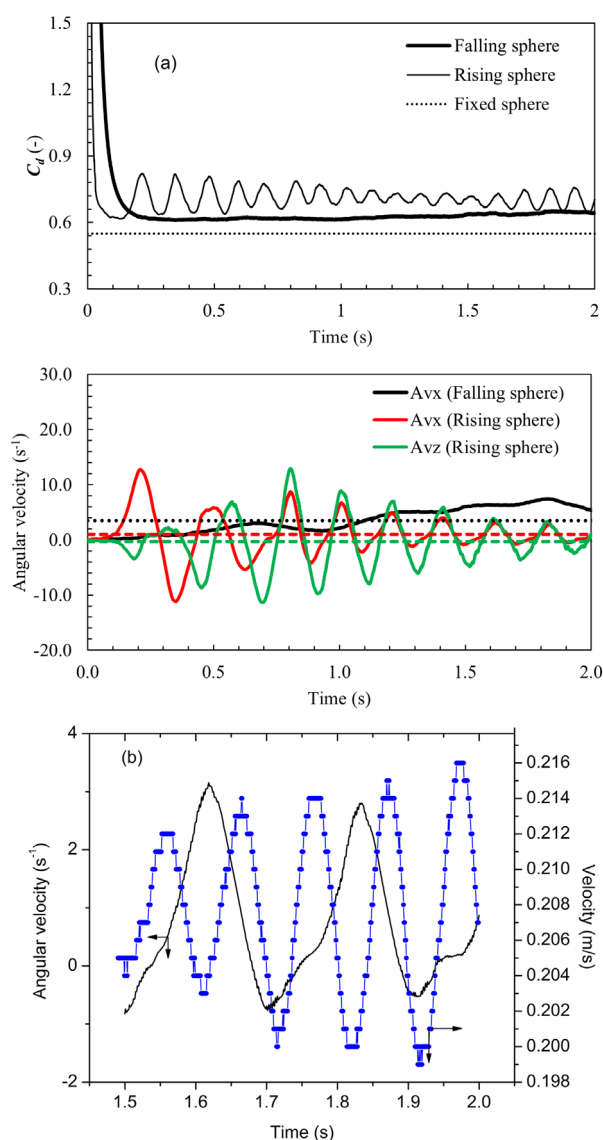


Figure 9. 3-D trajectories with y -directional velocity of a sphere falling in water at $\Delta\rho/\rho_f=0.7$ for different sphere diameters of 0.0025 m, 0.003 m, and 0.0035 m.

Table 2. Percentage deviation of time-averaged drag coefficient from the experimental studies

Study	Falling/Rising sphere	Density ratio ($\frac{\rho_p}{\rho_f}$)	Re_p	Maximum deviation in percentage	
				$\frac{ (C_d)_{\text{present}} - (C_d)_{\text{literature}} }{(C_d)_{\text{literature}}} \times 100$	
Veldhuis et al. ^[5]	Rising sphere	0.02* 0.08 ⁺	535–1035	8.6	
Horowitz and Williamson ^[6]	Rising sphere	$0 \leq \frac{\rho_p}{\rho_f} \leq 0.2^*$ $0.08 \leq \frac{\rho_p}{\rho_f} \leq 0.2^+$	535–1035	3	
	Rising sphere	$0.2 \leq \frac{\rho_p}{\rho_f} \leq 0.4^*$ $0.2 \leq \frac{\rho_p}{\rho_f} \leq 0.3^+$	478–1030	5	
Veldhuis et al. ^[5]	Falling sphere	1.4, 2.4 & 2.6* $1.7 \leq \frac{\rho_p}{\rho_f} \leq 1.92^+$	480–1091	20	
Boillat and Graf ^[14]	Falling sphere	$1.02 \leq \frac{\rho_p}{\rho_f} \leq 2.7^*$ $1.6 \leq \frac{\rho_p}{\rho_f} \leq 1.92^+$	200–1091	10	

*literature condition

⁺present condition**Figure 10.** Simultaneous variation of: (a) drag coefficient and angular velocity with time from rising and falling spheres at $\Delta\rho/\rho_f = 0.92$ and $D_p = 0.0025$ m; (b) x-directional angular velocity and y-directional velocity with time. Horizontal dotted lines are time-averaged values.

rising sphere, the effective increase in the drag coefficient is due to the non-vertical trajectory.

Initial Transient Drag Coefficients in the Rising and Falling Spheres

The transient drag coefficients are plotted by maintaining the density difference between fluid and sphere at the same level in the rising and falling cases at different sphere diameters (0.0025 m, 0.003 m, and 0.0035 m) as shown in Figures 10a–12a. To quantify the deviation between a fixed sphere and a freely moving sphere, the time-averaged drag coefficient value of a fixed sphere is also shown. That coefficient was calculated from Turton and Levenspiel's correlation by substituting the corresponding Re_p of the rising sphere. The transient drag coefficients were investigated in rising and falling spheres at the initial time period (0–0.1 s). In this regime, the sphere moved in a vertical path and its angular velocities were negligible (Figures 10a–12a). The pressure distribution around the sphere is axisymmetric (Figure 13a). Parameters such as dimensionless sphere surface pressure (C_p) and Darcy friction factor (f) along the right side of the hemisphere were plotted at different angular positions on the rising and falling sphere at 0.05 s (Figures 13b–c). C_p and f deviate significantly between a falling and rising sphere from 45° onwards until 180°, although the dimensionless density difference ($\Delta\rho/\rho_f$) between the fluid and sphere is the same (0.92). Hence, the flow field around the falling and rising sphere could not be unified at the initial time. The pressure loss and wall shear along the sphere surface are more prominent for the falling sphere than the rising sphere (Figures 13b–c). This can be a reason for the higher drag coefficient in falling spheres compared to rising spheres (Figures 10a–12a). From these results, we conclude that terminal velocity may be attained faster in the case of the rising sphere compared to the falling sphere, as shown in Figure 3.

Effect of Trajectory and Angular Velocity on the Transient Drag Coefficient

The x-directional angular velocity of the falling sphere and x- and z-directional angular velocities of the rising sphere are plotted with time as shown in Figures 10a, 11a, and 12a. When inspecting the drag coefficients at the initial time (time ~ 0), higher values were obtained in the rising and falling sphere and the

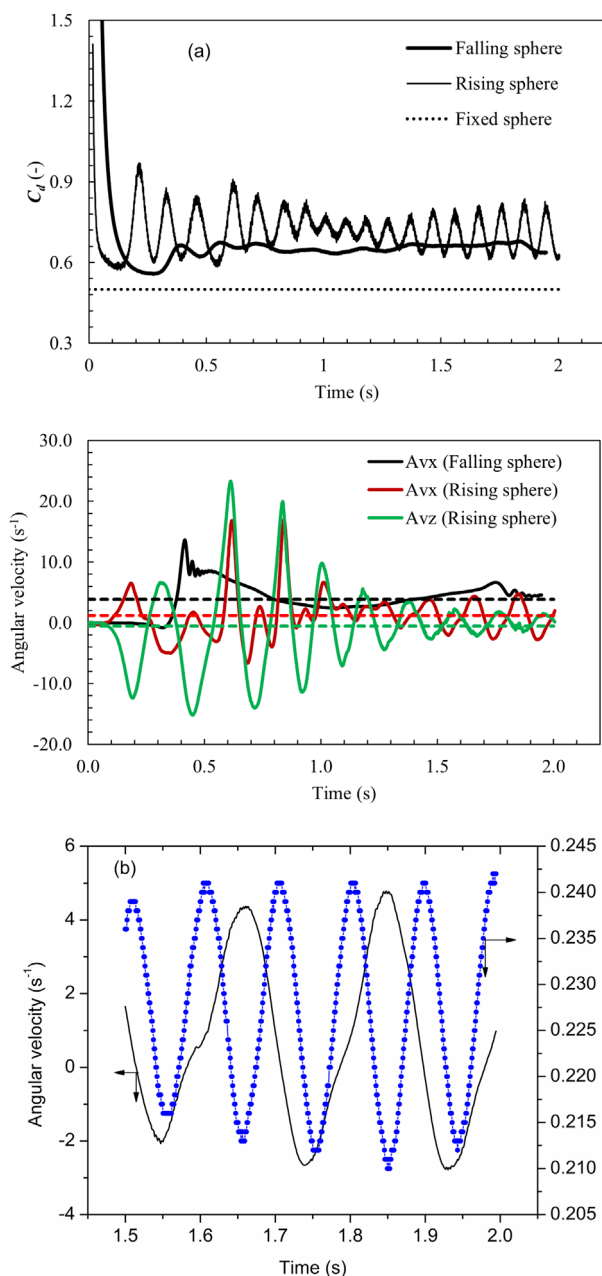


Figure 11. Simultaneous variation of: (a) drag coefficient and angular velocity with time from rising and falling spheres at $\Delta\rho/\rho_f=0.92$ and $D_p=0.003$ m; (b) x-directional angular velocity and y-directional velocity with time. Horizontal dotted lines are time-averaged values.

observations on the transient drag coefficient trends are summarized as follows.

Rising sphere

For the rising sphere, the drag coefficient drops faster with time and attained a minimum value. Further, the drag coefficient oscillated with time due to the dynamics of sphere movement and the interaction of the sphere with its wake. To understand the effects of trajectory, linear and angular velocities on transient drag coefficient, y-directional sphere velocity (against the gravity), and x-directional angular velocity were plotted with time after attaining steady oscillation for different sphere diameters (0.0025 m, 0.003 m, and 0.0035 m) at $\Delta\rho/\rho_f=0.92$ as shown in Figures 10b, 11b, and 12b.

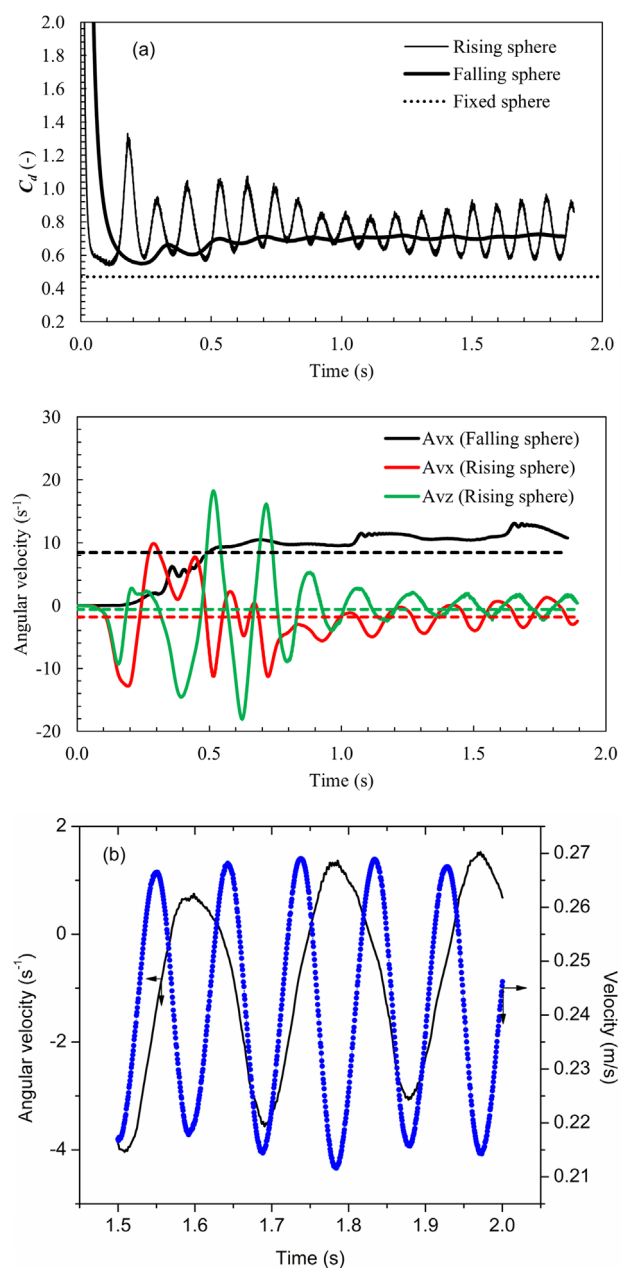


Figure 12. Simultaneous variation of: (a) drag coefficient and angular velocity with time from rising and falling spheres at $\Delta\rho/\rho_f=0.92$ and $D_p=0.0035$ m; (b) x-directional angular velocity and y-directional velocity with time. Horizontal dotted lines are time-averaged values.

When the sphere turns in a cycle of a helical path, the y-directional sphere velocity was at a maximum (Figure 6), the corresponding local drag coefficient was at a minimum (based on Equation (17)), and the x-directional angular velocity was at a minimum (close to zero; Figures 10b, 11b, and 12b). On the track of the trajectory, after the turn, the drag coefficient increases with a corresponding increase in angular velocity as shown in Figures 10b, 11b, and 12b. Both the drag coefficient and x-directional angular velocity of the rising sphere attained their relative maximum values at the middle of a cycle in the helical path, where the sphere velocity was lower. Further, the drag coefficient and angular velocity were relatively lower when the sphere moved further from the middle of a cycle of helical path as shown in Figures 10b, 11b, and 12b. The time-averaged

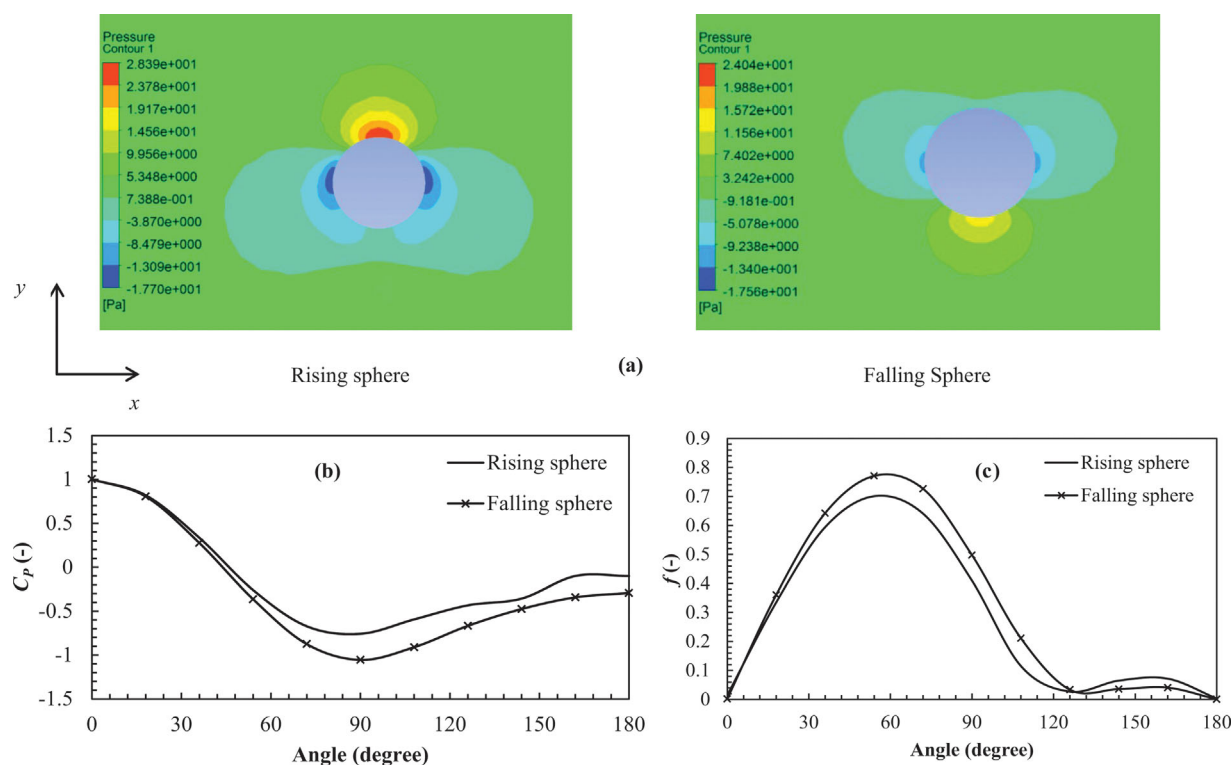


Figure 13. Comparison of: (a) pressure distribution around the sphere, (b) dimensionless sphere surface pressure, (c) Darcy friction factor in rising and falling spheres at 0.05 s and $\Delta\rho/\rho_f = 0.92$.

x -directional angular velocities for different sphere diameters were significantly lower in the rising sphere compared to the falling sphere angular velocities (Figures 10a, 11a, and 12a). From this result, it is clear that the transient drag coefficient deviates from the standard drag coefficient due to significant trajectory deviation from vertical motion (Figures 6 and 8).

Falling sphere

The initial value of the drag coefficient dropped slowly with time compared to the rising sphere for different sphere diameters (Figures 10a, 11a, and 12a). It showed an oscillatory behaviour and stabilized with time once the minimum value was attained. These behaviours can be synchronized with x -directional angular velocities with time, which are shown in Figures 10a, 11a, and 12a. Similar trends in the velocity of falling spheres in water were reported by Mordant and Pinton.^[15] From the above observation we conclude that the drag coefficients deviate from the standard value due to a significant level of angular

velocity in a falling sphere in water. This may be a reason for the higher time-averaged drag coefficient compared to the standard drag coefficient, which is also confirmed by data from Boillat and Graf.^[14]

Residence Time of the Rising and Falling Sphere

Comparison of residence times from falling, rising, and fixed sphere cases appears in Table 3. They were calculated by the sphere travelling a fixed distance of 0.45 m for two different $\Delta\rho/\rho_f$ values (0.7 and 0.92) and different sphere diameters. The procedure used to estimate the residence time for fixed sphere case is discussed elsewhere.^[12] Note that the residence time decreased with increasing sphere diameter at given $\Delta\rho/\rho_f$ for all the cases of falling, rising, and fixed spheres. The residence time of rising spheres was slightly greater than that of falling spheres at a given $\Delta\rho/\rho_f$ of 0.92. This may be attributed to the higher drag coefficient of rising spheres compared with falling spheres (Figure 4).

Table 3. Comparison of residence time of rising and falling spherical particles in a fluid for fixed sphere case

Particle diameter (m)	Particle Reynolds number (Re_p)		$\Delta\rho/\rho_f$	Residence time (s)		
	Falling	Rising		Falling	Rising	Fixed sphere
0.0025	480.6	478.5	0.7	2.49	2.49	2.31
	571	535.7	0.92	2.1	2.22	1.98
0.003	644.4	635.6	0.7	2.23	2.23	2.03
	738.4	702.7	0.92	1.95	2	1.76
0.0035	799.1	799.1	0.7	2.1	2.1	1.84
	903	865	0.92	1.85	1.91	1.61
0.004	962.5	962.5	0.7	1.99	1.96	1.7
	1091.3	1035.4	0.92	1.75	1.8	1.49

CONCLUSIONS

The arbitrary Lagrangian-Eulerian moving mesh simulation technique was successfully implemented in the present study up to a maximum Re_p of 1091 using ANSYS CFX[®]CFD software, and the results obtained were validated with experimental data available in the literature.

For higher particle Reynolds numbers > 1000 , very fine mesh and a small time step are essential to capture the particle motion inside the domain. Commercial ANSYS CFX V13[®] may be sufficient to study particle dynamics in fluid with a high Reynolds number. However, supercomputing facilities and/or a suitable selection of turbulence modelling are essential to show the high-resolution dynamics of particle motion and the interaction of the wake structure of a fluid around a particle.

The trajectories of the rising and falling spheres were different even when $\Delta\rho/\rho_f$ and sphere diameter were the same. The angular velocity was significantly higher in the falling sphere compared to the rising sphere, which led to a higher deviation of the drag coefficient from the standard drag coefficient. The large pressure loss and friction factor around the sphere at the initial transient motion of the falling sphere delayed the terminal velocity of the falling sphere compared with the rising sphere. The methodology used in this study might be refined further for different particle shapes and be extended to multiple particles in stagnant fluid.

NOMENCLATURE

C_d	local drag coefficient
$\langle C_d \rangle$	time-averaged drag coefficient
C_p	dimensionless surface pressure of sphere
D_p	diameter of the sphere (m)
D_t	width or breath of the duct (m)
D_x	displacement of sphere in x -direction
D_y	displacement of sphere in y -direction
D_z	displacement of sphere in z -direction
f	Darcy friction factor
g	acceleration due to gravity (m/s^2)
m	mass of the sphere (kg)
P	pressure (Pa)
P_s	sphere surface pressure (Pa)
Re_p	particle Reynolds number
u_t	terminal velocity of sphere (m/s)
$\langle u_t \rangle$	time-averaged terminal velocity of sphere (m/s)
U_p	translational velocity (m/s)
V	velocity (m/s)
V_s	front stagnation velocity (m/s)
X	dimensionless displacement of sphere in x -direction
Y	dimensionless displacement of sphere in y -direction
Z	dimensionless displacement of sphere in z -direction

Greek Letters

∇	del operator
μ	viscosity of water ($\text{kg/m} \cdot \text{s}$)
ρ_f	density of water (kg/m^3)
ρ_p	density of sphere (kg/m^3)
τ_{ij}	shear stress (Pa)
Ω	angular velocity (rad/s)

REFERENCES

- [1] D. G. Karamanerv, L. N. Nikolov, *AIChE J.* **1992**, *38*, 1843.
- [2] T. Renganathan, K. Krishnaiah, *Can. J. Chem. Eng.* **2003**, *81*, 835.

- [3] D. F. Lawler, P. C. Singer, C. R. O' Melia, *Res. J. Water Pollut. C* **1982**, *54*, 1388.
- [4] S. S. Rabha, V. V. Buwa, *Ind. Eng. Chem. Res.* **2010**, *49*, 10615.
- [5] C. Veldhuis, A. Biesheuvel, D. Lohse, *Int. J. Multiphas. Flow* **2009**, *35*, 312.
- [6] M. Horowitz, C. H. K. Williamson, *J. Fluid. Mech.* **2010**, *651*, 251.
- [7] H. H. Hu, N. A. Patankar, M. Y. Zhu, *J. Comput. Phys.* **2001**, *169*, 427.
- [8] B. H. Yang, J. Wang, D. D. Joseph, H. H. Hu, T. W. Pan, R. Glowinski, *J. Fluid Mech.* **2005**, *540*, 109.
- [9] N. A. Quddus, W. A. Moussa, S. Bhattacharjee, *J. Colloid Interf. Sci.* **2008**, *317*, 620.
- [10] R. Turton, O. Levenspiel, *Powder Technol.* **1986** *47*, 83.
- [11] P. P. Brown, D. F. Lawler, *J. Environ. Eng.* **2003**, *129*, 222.
- [12] N. S. Cheng, *Powder Technol.* **2009** *189*, 395.
- [13] K. R. Rupesh, J. B. Joshi, K. Nandhakumar, P. D. Minev, *Chem. Eng. Sci.* **2010**, *65*, 2159.
- [14] J. L. Boillat, W. H. S. Graf, *J. Hydraul. Eng.-ASCE* **1981**, *107*, 1123.
- [15] N. Mordant, J. F. Pinton, *Eur. Phys. J. B* **2000**, *18*, 343.
- [16] M. Jenny, G. Bouchet, J. Dušek, *Phys. Fluids* **2003**, *15*, L9.
- [17] M. Jenny, J. Dušek, G. Bouchet, *J. Fluid Mech.* **2004**, *508*, 201.
- [18] H. Niazmand, M. Renksizbulut, *Comput. Fluids* **2003**, *32*, 1405.
- [19] ANSYS Inc., *Ansyes CFX Documentation*, ANSYS Inc., Canonsburg **2000**.
- [20] C. M. Rhie, W. L. Chow, *AIAA J.* **1983**, *21*, 1525.
- [21] K. Neeharika, A. Kannan, M. U. S. V. Aditya Varadhan, *Food Bioprocess Tech.* **2011**, *4*, 429.
- [22] J. C. Simo, K. K. Wong, *Int. J. Numer. Meth. Eng.* **1991**, *31*, 19.
- [23] S. Krishnan, A. Kannan, *Engineering Applications of Computational Fluid Mechanics* **2010** *4*, 396.
- [24] P. Bagchi, M. Y. Ha, S. Balachander, *J. Fluid. Eng.-T. ASME* **2001**, *123*, 347.

Manuscript received May 30, 2015; revised manuscript received September 5, 2015; accepted for publication October 11, 2015.